


## Insights into the origin of robust ferroelectricity in HfO<sub>2</sub>-based thin films from the order-disorder transition driven by vacancies

Chenxi Yu,<sup>1,2,‡</sup> Haili Ma,<sup>1,2,‡</sup> Mingqiang Li,<sup>3,‡</sup> Fei Liu,<sup>1,2,\*</sup> Xiangxiang Ding,<sup>1,2</sup> Yudi Zhao,<sup>1,2</sup> Haolin Li,<sup>1,2</sup> Xujin Song,<sup>1,2</sup> Fachen Liu,<sup>3</sup> Wanwang Yang,<sup>1,2</sup> Jun Xu,<sup>3</sup> Jingmin Zhang,<sup>3</sup> Xiaorui Hao,<sup>3</sup> Lifeng Liu<sup>①</sup>,<sup>1,2</sup> Peng Huang,<sup>1,2</sup> Peng Gao,<sup>3</sup> and Jinfeng Kang<sup>1,2,†</sup>

<sup>1</sup>*School of Integrated Circuits, Peking University, Beijing, China*

<sup>2</sup>*Beijing Advanced Innovation Center for Integrated Circuits, Peking University, Beijing, China*

<sup>3</sup>*Electron Microscopy Laboratory, School of Physics, Peking University, Beijing, China*

 (Received 16 March 2024; revised 7 June 2024; accepted 16 July 2024; published 9 August 2024)

HfO<sub>2</sub>-based ferroelectrics (FE-HfO<sub>2</sub>) have triggered extensive research interest because they are promising materials for beyond-Moore electronic device applications. However, the origin of ferroelectricity in HfO<sub>2</sub>-based ferroelectrics remains elusive. Here, we demonstrate that the ordered oxygen vacancies (V<sub>O</sub>) in FE-HfO<sub>2</sub> thin films contribute to ferroelectricity through the formation of a stable-polar phase. In FE-HfO<sub>2</sub> thin films, oxygen vacancy (V<sub>O</sub>) defects induce local electric dipoles and the ordered V<sub>O</sub> distribution results in the stable-polar phases. Using first-principles calculations, a thermodynamically stable-polar phase *M*<sub>1</sub> with the spontaneous polarization of 27 μC/cm<sup>2</sup> is predicted in monocliniclike Hf<sub>4</sub>Zr<sub>4</sub>O<sub>15</sub> structures. Moreover, the predicted *M*<sub>1</sub> structures are directly visualized in Hf<sub>0.5</sub>Zr<sub>0.5</sub>O<sub>2-δ</sub> (HZO) ferroelectric thin films using spherical aberration (Cs)-corrected scanning transmission electron microscopy. The proposed mechanism for V<sub>O</sub>-induced order-disorder ferroelectricity in FE-HfO<sub>2</sub> opens a new pathway to explore the underlying physics of the ferroelectric characteristics in FE-HfO<sub>2</sub>.

DOI: [10.1103/PhysRevApplied.22.024028](https://doi.org/10.1103/PhysRevApplied.22.024028)

### I. INTRODUCTION

The discovery of ferroelectricity in doped HfO<sub>2</sub> thin films [1] has triggered extensive research interest due to the excellent scalability and compatibility with modern CMOS technology [2–4]. The robust ferroelectricity has been widely demonstrated in FE-HfO<sub>2</sub>, even undergoing more than 10<sup>11</sup> times switching cycling [5,6] or at an ultrathin thickness of less than 3 nm [3,7]. Various theoretical calculations and experimental studies have been carried out to investigate the underlying physical mechanisms of FE-HfO<sub>2</sub> ferroelectricity [8–33]. Up to now, the ferroelectricity of FE-HfO<sub>2</sub> is generally attributed to the formation of a metastable polar orthorhombic phase (space group *Pca*2<sub>1</sub>, named *o*-FE) [8–11]. Tremendous work has been performed to identify the critical factors to stabilize the metastable *o*-FE phase, taking account of various effects such as dopants [12–18], grain boundary [19,20], strain [21], interface [22,23], V<sub>O</sub> concentration [24–31], and fabrication process conditions [32, 33]. However, the related physical explanations are still

questionable and elusive. As summarized in a comprehensive review article by Schroder *et al.* [34], various theoretical investigations have revealed that the thermodynamic stabilization of the ferroelectric *o*-phase with *Pca*2<sub>1</sub> symmetry is unlikely. The reasonable physical explanations for the experimentally observed ferroelectricity based on the *o*-FE theory require kinetically limited fabrication conditions. However, numerous studies indicated that it is quite an easy task to realize robust ferroelectricity in various HfO<sub>2</sub>-based ferroelectric films or devices [14–16,33]. Recently, other polar phases were reported to contribute to the robust ferroelectricity beyond the *o*-FE phase, such as monoclinic phase in oxygen-deficient HfO<sub>2</sub> [29] and rhombohedral phase in Hf(Zr)-excess Hf(Zr)<sub>1+x</sub>O<sub>2</sub> [35]. These facts imply that it is necessary to explore a new physical principle beyond the *o*-FE phase formation theory to elucidate the essential origin of ferroelectricity in FE-HfO<sub>2</sub>. Recently, the close relation between oxygen vacancies and ferroelectricity has been demonstrated, although the underlying mechanism remains elusive [24–31]. We propose that the ordered V<sub>O</sub> in HfO<sub>2</sub> thin films contribute to ferroelectricity through the formation of stable ferroelectric phases by order-disorder transition, which can account for the robust ferroelectricity in HfO<sub>2</sub>-based thin films with various dopants under different fabrication processes.

\*Contact author: Feiliu@pku.edu.cn

†Contact author: Kangjf@pku.edu.cn

‡These authors contributed equally: Chenxi Yu, Haili Ma, and Mingqiang Li.

## II. OXYGEN VACANCY INDUCED FERROELECTRICITY

A basic assumption of the *o*-FE phase formation theory is that the ferroelectricity of HfO<sub>2</sub>-based ferroelectrics results from the structural transition from a centrosymmetric nonpolar paraelectric phase to a noncentrosymmetric polar one through the displacement of oxygen anions from the Hf cations in the lattices of the stoichiometric HfO<sub>2</sub>-based materials. This means that the *o*-FE HfO<sub>2</sub> is classified as displacive ferroelectrics similar to some of the most common perovskite-type ferroelectrics. Such an assumption and derived conclusions are reasonable for the stoichiometric HfO<sub>2</sub>-based crystalline materials without defects. However, it is well-known that the existence of V<sub>O</sub> is intrinsic in HfO<sub>2</sub>-based thin films [28,36]. First-principles calculations show that V<sub>O</sub> has the lowest formation energy under low oxygen partial pressure [37,38]; therefore, V<sub>O</sub> is the dominant defect under practical conditions. Various theoretical and experimental results have demonstrated that the ferroelectric properties of FE-HfO<sub>2</sub>, especially the polarization switching behaviors, are strongly correlated with the distribution and dynamic behavior of V<sub>O</sub> [24–31]. In our previous study [31], first-principles calculations based on density functional theory (DFT) indicate that V<sub>O</sub> in the supercells of the monoclinic HfO<sub>2</sub> (space group  $P2_1/c$ , named *m*-phase) can induce localized electric dipoles with different magnitudes and directions at different locations. Electric cycling behavior can be explained by the dynamic behavior of V<sub>O</sub> under an applied electric field. Similarly, Rushchanskii *et al.* studied the ordering pattern of V<sub>O</sub> in substoichiometric HfO<sub>2- $\delta$</sub>  [29]. Based on first-principles calculations, they predicted a monoclinic phase in substoichiometric HfO<sub>2- $\delta$</sub>  with spontaneous polarization. These theoretical results seem to indicate that the properties of intrinsic V<sub>O</sub> defects in HfO<sub>2</sub>-based thin films are similar to cation ions such as H<sup>+</sup> or vacancy defects in the typical order-disorder ferroelectrics [39–41], such as the KH<sub>2</sub>PO<sub>4</sub> (KDP) family [39] or dipole glasses [41]. In typical order-disorder ferroelectrics, ferroelectricity results from the ordering transition of the permanent electric dipoles induced by the cation ions or vacancy defects from the disordered state to the ordered state. For HfO<sub>2</sub>-based ferroelectrics, we propose that the intrinsic V<sub>O</sub> induces localized dipoles, which contribute to robust ferroelectricity through the formation of a stable ferroelectric phase via an order-disorder transition. Based on the mechanism of V<sub>O</sub>-induced ferroelectricity, we can deduce that annealing and wakeup processes are beneficial to the ordering of vacancies that, as a consequence, strengthen ferroelectricity in HfO<sub>2</sub> thin films, as confirmed in previous reports [13,42]. The migration of vacancies under an applied electric field [28] and the enhanced ferroelectricity under oxygen-deficient conditions [34] can also be naturally explained.

To quantify the measured ferroelectric characteristics of various FE-HfO<sub>2</sub> devices, we developed a physical model based on the proposed assumption. In the proposed physical model, the dynamic behaviors of FE-HfO<sub>2</sub> systems are assumed to obey the Ginsburg-Landau-Devonshire-type theory for ferroelectrics [43], which is described by a double-well potential model of free energy landscape  $F$  as a function of the polarization  $P$  [Fig. 1(a)]. In Ginsburg-Landau-Devonshire theory, free energy is expanded by order parameter. For ferroelectrics, electric polarization  $P$  is the order parameter that changes during phase transition. The two degenerate energy minima [Fig. 1(a)] define two stable spontaneous polarization states ( $\pm P_r$ ) of a thermodynamically stable phase, which can be reversed under an applied electric field. Here, V<sub>O</sub> in FE-HfO<sub>2</sub> breaks the central symmetry in most of the nonferroelectric phases, such as monoclinic and tetragonal phases. The symmetry breaking caused by the formation of V<sub>O</sub> induces localized dipoles [Fig. 1(b)] of which the orientations are related to the positions of V<sub>O</sub> in the crystal [Fig. 1(c)]. We assume that V<sub>O</sub> distribution is ordered in the ferroelectric phase while disordered in the paraelectric phase [Fig. 1(d)]. Furthermore, we can develop corresponding theoretical calculation methods to identify the polar phases and the critical impact factors for the formation of a stable ferroelectric phase in HfO<sub>2</sub>-based oxides. The stable ferroelectric polar phase of a given FE-HfO<sub>2</sub> system can be identified on the assumption that V<sub>O</sub> has an ordered distribution, taking account of various correlated factors such as the concentration of V<sub>O</sub> and dopants, strain, surface and interface, or electrodes. DFT calculations are an effective and efficient method to identify the stable ferroelectric polar phase. Once the stable ferroelectric polar phase is obtained, the ferroelectric properties can be easily determined, including polarization states, spontaneous polarization, and switching pathways.

## III. DENSITY FUNCTIONAL CALCULATIONS

To verify the validity of the proposed physical principle and theoretical calculation methods for the identification of the stable-polar phase in FE-HfO<sub>2</sub>, the corresponding theoretical calculations and experimental verifications for a given Hf<sub>0.5</sub>Zr<sub>0.5</sub>O<sub>2- $\delta$</sub>  (HZO) system were sequentially carried out. For the theoretical calculations, we first studied the structural properties of the substoichiometric HZO by DFT-based first-principles calculations combined with an evolutionary algorithm, using the Vienna *ab initio* simulation package (VASP) [44,45] and USPEX code [46,47]. Vacancies in substoichiometric Hf<sub>0.5</sub>Zr<sub>0.5</sub>O<sub>2- $\delta$</sub>  introduce in-gap states and a large density of in-gap states may lead to extensive leakage. The density of in-gap states decreases as V<sub>O</sub> concentration decreases, as discussed in Fig. S2 in the Supplemental Material [48]. We determined that a concentration corresponding to  $\delta = 0.125$  is reasonable

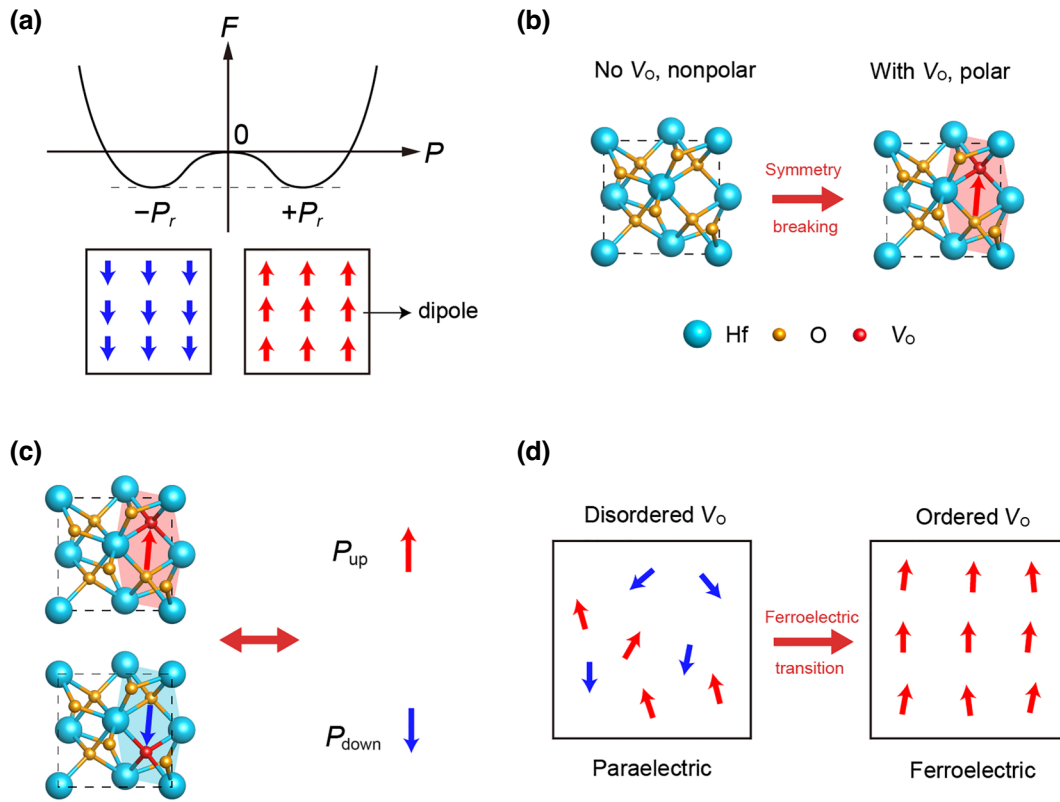


FIG. 1. Proposed order-disorder behavior of ferroelectric  $\text{HfO}_2$  due to vacancy ordering transition. (a) Free energy (vertical axis  $F$ ) versus electric polarization (horizontal axis  $P$ ) graph showing a double-well potential shape in the ferroelectric state, in which polarization states with positive and negative polarization are located in two valleys. The black square with arrows shows the direction of localized dipoles of ferroelectrics in the ferroelectric state. Red arrows are dipoles pointing upward and blue arrows are dipoles pointing downward. For order-disorder ferroelectrics, dipoles are maximally ordered in the ferroelectric state. (b) In  $\text{HfO}_2$ -based ferroelectrics, intrinsic oxygen vacancies induce localized dipoles by symmetry breaking. This mechanism is not limited to the monoclinic  $\text{HfO}_2$  phase, which is used for demonstration. (c) Dipole direction relating to the position of  $V_{\text{O}}$ , where upward and downward dipoles ( $P_{\text{up}}$  and  $P_{\text{down}}$ ) and corresponding  $V_{\text{O}}$  positions in the cells are demonstrated. (d) Transition from disordered paraelectric state to ordered ferroelectric state, i.e., a disorder-order transition, in which the disordered dipoles are aligned to a certain direction. The  $\text{HfO}_2$  phases with disordered dipoles are paraelectric, while the  $\text{HfO}_2$  phases with ordered dipoles are ferroelectric (as shown in the figure).

in FE-HZO thin films. Thus, we performed an extensive study of the  $\text{Hf}_{0.5}\text{Zr}_{0.5}\text{O}_{2-\delta}$  stoichiometry with  $\delta = 0.125$  and made a comparison among all the oxygen-deficient phases.

An HZO unit cell with one  $V_{\text{O}}$  in 24 atoms is first constructed to search for the possible atomic configurations distinguished by the local  $V_{\text{O}}$  arrangements. Oxygen-deficient monoclinic ( $m$ ), orthorhombic ( $o$ ), and tetragonal ( $t$ ) phases (space group  $P4_2/nmc$ , named tetragonal phase) are constructed as initial structures for structure searching. The latter uses the evolutionary algorithm implemented in the USPEX code [46,47]. For each generation in the evolutionary algorithm, 60% of the structures with the lowest energy were used to produce the next generation, and 50 generations were simulated. Offspring structures in the next generation were produced using the operators implemented in USPEX [49]. Detailed methods for structure searching are shown in the Appendix A 1. The resulting

oxygen-deficient phases are grouped by their structural similarity to the stoichiometric HZO phases. There are four groups of oxygen-deficient phases (three of which are introduced above): monoclinic, orthorhombic, tetragonal, and distorted tetragonal ( $dt$ ) phases. The total energy versus volume diagram for all the oxygen-deficient phases is presented in Fig. 2(a), where the lowest energy is achieved in the monoclinic  $M_1$  phase. The atomic structures of the relevant phases are shown in Fig. S1 in the Supplemental Material [48].

The molecular dynamics simulation via CP2K [50] indicates that the  $M_1$  structure is dynamically stable at room temperature [Fig. 2(b)]. Therefore, the  $V_{\text{O}}$  ordering in the atomic structures of the  $M_1$  phase is the preferred form in  $\text{Hf}_{0.5}\text{Zr}_{0.5}\text{O}_{2-\delta}$  thin films compared with other phases under certain practical conditions. It is well-known that the stoichiometric monoclinic HZO phase ( $M_0$ ) is nonpolar without spontaneous polarization. However, electronic

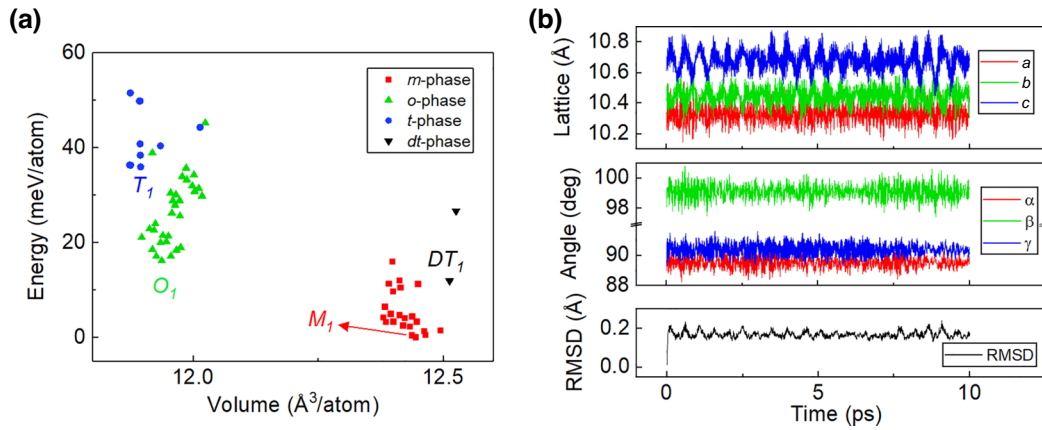


FIG. 2. Structure searching for the stable ferroelectric phase in  $\text{Hf}_{0.5}\text{Zr}_{0.5}\text{O}_{2-\delta}$ . (a) Energy as a function of the volume of  $\text{Hf}_{0.5}\text{Zr}_{0.5}\text{O}_{2-\delta}$  crystalline structures obtained from the evolutionary algorithm. The resulting oxygen-deficient phases are grouped into four groups: the  $m$ ,  $o$ ,  $t$ , and  $dt$  phases. The  $M_1$ ,  $O_1$ ,  $T_1$ , and  $DT_1$  phases are the lowest energy phases of the  $m$ ,  $o$ ,  $t$ , and  $dt$  phases, respectively. The  $dt$  phase is a distorted tetragonal phase with large lattice distortion. The  $M_1$  phase has the lowest energy of all the phases. (b) Molecular dynamics simulation indicating that the  $M_1$  phase is dynamically stable at 300 K. Small changes in the lattice constants, angles between lattice vectors, and small root-mean-square deviations (RMSD) during the simulation indicate that no phase transition occurs for the simulation time of 10 ps.

polarization can be induced by  $V_O$  due to central symmetry breaking and the ordered distribution of  $V_O$  gives rise to macroscopic ferroelectric polarization. Two polarization states of the  $M_1$  phase and the polarization switching path are demonstrated in Fig. 3. Localized dipoles induced by  $V_O$  are aligned and separated by nonferroelectric (nonFE) layers. The localized dipoles and nonferroelectric layer in the  $M_1$  phase are similar to the polar cell and spacer layer in the orthorhombic phase, as reported in Ref. [11], which indicates that the robustness of ferroelectricity in nanoscale  $\text{HfO}_2$  may originate from the structural

characteristics of ferroelectric phases that are substantially different from the continuous polarization distributions in perovskite ferroelectric phases.

Our calculations demonstrate that the theoretical polarization of the  $M_1$  phase is  $P_r = 27 \mu\text{C}/\text{cm}^2$  [Fig. 4(a)] using Berry phase methods implemented in VASP [44,45] along the switching path in Fig. 3, which is close to the reported results [51,52]. Therefore, it is reasonable to conclude that the formation of the  $V_O$ -ordered  $M_1$  phase and the switching between the two stable polarization states are responsible for ferroelectric behaviors observed in

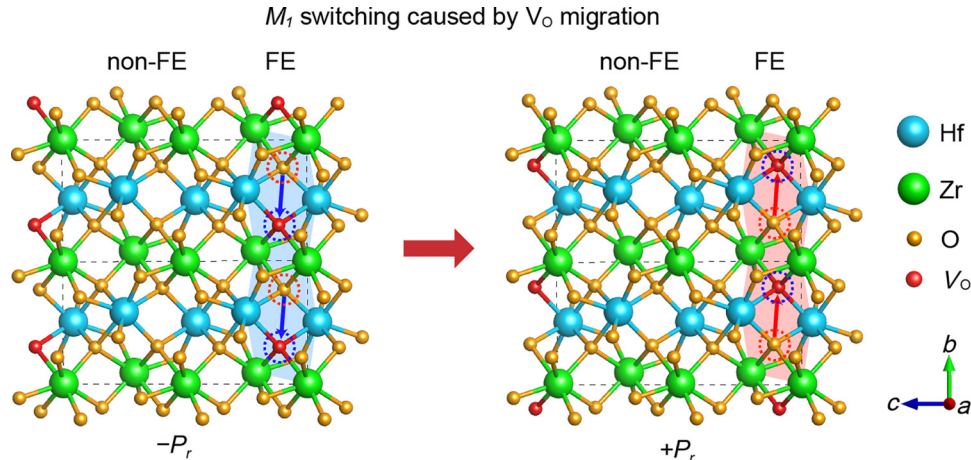


FIG. 3. Crystalline structure and switching mechanism of the  $M_1$  phase. Here,  $V_O$  is highlighted using red balls and blue dashed circles. The  $M_1$  phase consists of ferroelectric (FE) layers and nonferroelectric (non-FE) layers. Localized dipoles induced by  $V_O$  are located in FE layers and are separated by non-FE layers, which leads to robust ferroelectricity in  $\text{HfO}_2$ . Polarization switching is caused by the migration of  $V_O$  in the  $M_1$  phase to the adjacent oxygen position, highlighted by a red dashed circle (or, equivalently, the migration of oxygen atoms to the adjacent  $V_O$ ). The final structure on the switching path is the spatial reversal of the  $M_1$  phase.

FE-HZO. The electronic polarization switching is associated with the transition between the  $V_O$ -ordered  $M_1$  structure and its spatial reversal, accompanied by the  $V_O$  exchange between neighboring asymmetrical sites that correspond to the polarization reversal (Fig. 3). The energy as a function of  $V_O$  reaction coordinates along the polarization switching path from  $-P_r$  to  $+P_r$  is also plotted [Fig. 4(b)]. The calculated barrier of the polarization switching is about 51 meV/atom based on the oxygen atom diffusion model by the VTST package [53,54]. The real switching path may have a lower barrier impacted by various factors. One of these factors is the ordering transition of  $V_O$  during the switching process. We found a possible path with a switching barrier of 25 meV/atom (Fig. S3 in the Supplemental Material [48]), in which the ordered  $V_O$  becomes disordered during switching and returns to the ordered state after switching. Another factor is the charge effect, where the ferroelectric switching barrier is lowered if vacancies are charged [55,56]. We calculated the effect of charged vacancies and found that the barrier of the path, in Fig. S3 in the Supplemental Material [48], lowers to 15 meV/atom if vacancies are charged.

Other factors include the displacement or tunneling of oxygen atoms (O) or ions ( $O^{2-}$ ), drift and diffusion, or generation and recombination of  $V_O$  with  $O^{2-}$  similar to the switching process occurring in resistive switching devices [27–30]. On supposing that the dynamic behaviors are dominated by the stochastic generation and recombination of  $V_O$ , the similarity of switching behaviors between FE-HfO<sub>2</sub> devices and resistive switching devices can be expected, as reported in previous publications [25,57–59]. In this case, the key ferroelectric switching parameters, such as the coercive field  $E_c$ , can be determined by the parameters associated with the generation and recombination or diffusion of  $V_O$  in FE-HfO<sub>2</sub>. It should be noted that the above DFT calculations are only based on the fixed

concentrations of dopant and  $V_O$  without surface and interface or electrode. Other factors, such as the surface and interface or electrode, different dopants, and different concentrations of dopant and  $V_O$ , may result in the various stable-polar phases, as discussed in Appendix E.

#### IV. EXPERIMENTAL CHARACTERIZATION

Next, the corresponding experimental verification of the  $V_O$ -ordered stable-polar  $M_1$  phase predicted by the theory calculations was performed. The transmission electron microscopy (TEM) technique is an effective method to characterize the phase structure and ferroelectric properties of HfO<sub>2</sub> thin films [60]. The combined electron microscopy techniques, including high-resolution transmission electron microscopy (HRTEM), aberration-corrected scanning transmission electron microscopy (STEM), and electron energy-loss spectroscopy (EELS), were sequentially implemented to detect  $M_1$  structures in the fabricated FE-HZO samples, in which the typical robust ferroelectric switching behaviors were measured [Figs. 5(a) and S6 in the Supplemental Material [48]]. The use of high spatial resolution and easily accessible HRTEM can not only help us identify the monoclinic structures (of both perfect  $M_0$  without oxygen vacancy and  $M_1$ ) in polycrystalline HZO thin films rapidly, but also provide some basic sample information such as morphology, thickness, grain size, and even crystal quality, etc. For example, the diameter of our FE-HZO grains is 15–20 nm according to the HRTEM images (Fig. S7 in the Supplemental Material [48]). In addition, some more detailed structural features and the oxygen-deficient status of FE-HZO thin films need to be further characterized via Cs-STEM and EELS. We note that it is a challenging task to identify the targeted  $M_1$  structures in the ultrathin FE-HZO layers with the mixed and complex polymorphic

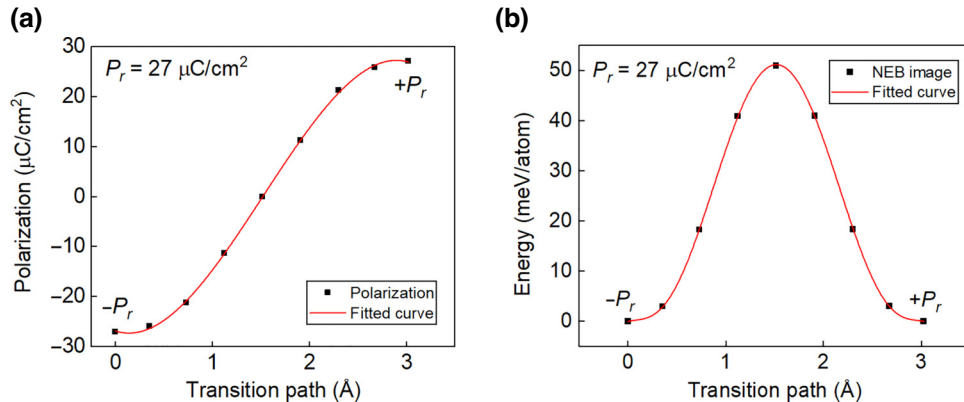


FIG. 4. Electronic polarization and switching path of the  $M_1$  phase. (a) Polarization as a function of oxygen vacancy ( $V_O$ ) reaction coordinates along the polarization switching path in Fig. 3 from  $-P_r$  to  $+P_r$ . The spontaneous polarization  $P_r$  is calculated as 27  $\mu\text{C}/\text{cm}^2$ . (b) Energy along the polarization switching path in Fig. 3. The switching potential has a double-well shape for an order-disorder type ferroelectric system.

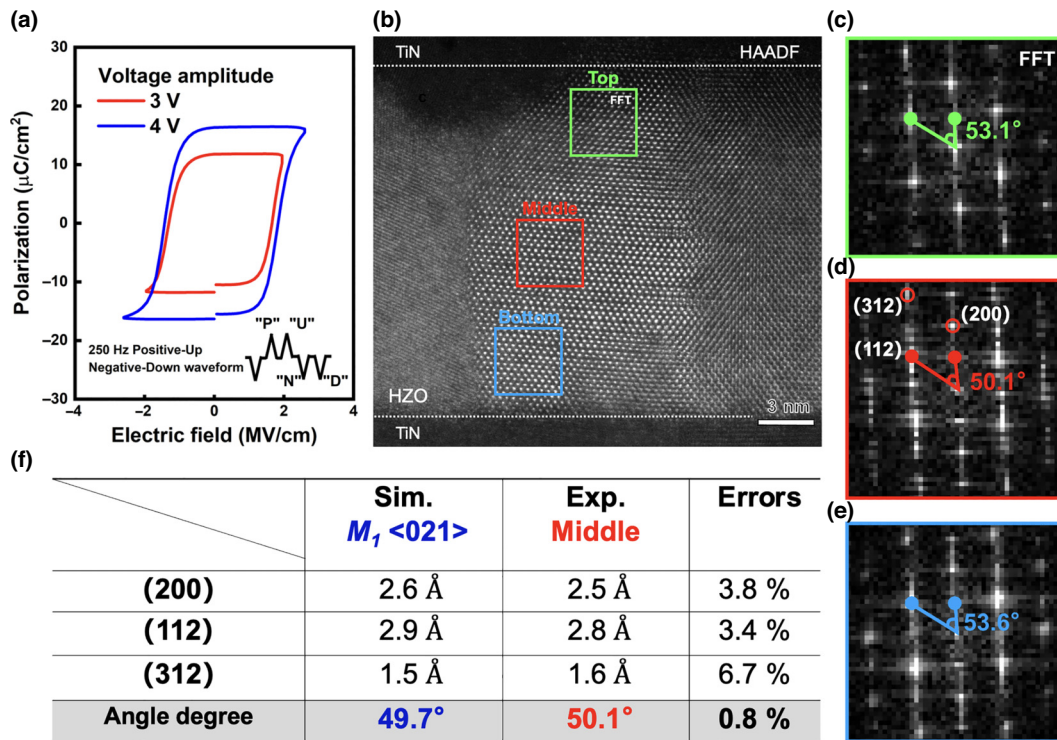


FIG. 5. Selection for monoclinic structures in polycrystalline FE-HZO thin films. (a) Measured  $P$ - $V$  curves in the device of TiN (30 nm)/ $\text{Hf}_{0.5}\text{Zr}_{0.5}\text{O}_{2-\delta}$  (15 nm)/TiN (40 nm) by the PUND measurement method. The typical ferroelectric loop behaviors were observed. (b) HAADF image of the aligned HZO grain located at the thinnest FIB area (Fig. S10 in the Supplemental Material [48]). (c)–(e) FFT patterns taken from the top, middle, and bottom parts of the experimental HAADF image shown in (b), respectively. (f) Comparison between lattice parameters of  $\langle 021 \rangle$ -oriented  $M_1$  model and experimental measurements. Note that the middle parts of the aligned HZO grain effectively match with the  $M_1$  structures along the  $\langle 021 \rangle$ -direction, while the parts close to the top or bottom electrode have totally different structures due to their large angle deviations. Based on our findings, it can be reasonably conjectured that the surface and interface, or electrode and oxygen vacancy ( $V_O$ ) accumulations, may heavily affect HZO structures.

phase structures due to the weak scattering of oxygen atoms. Fortunately, the integrated and differentiated differential phase contrast (iDPC/dDPC) STEM techniques could be employed to obtain local electrostatic potential field and charge density distribution of the thin sample, which are able to directly identify oxygen atomic columns in FE-HZO thin films with higher spatial resolution and without the limitation of specimen geometry, offering a new method to solve this challenging issue [61–63].

In our FE-HZO layers, we noticed that a number of virgin grains in HRTEM images feature that contains a double-modulated stacking with an inclined orientation, which seems to have monoclinic HZO structures (Figs. S8 and S9 in the Supplemental Material [48]). Therefore, these kinds of featured structures and corresponding electron diffraction patterns can be used as indicators for the preliminary selection of monoclinic HZO structures in the polycrystalline FE-HZO layers. It is experimentally found that most of these monoclinic HZO structures in our FE-HZO layers are near or can be aligned toward the  $\langle 021 \rangle$ -zone axes. Note that the  $\langle 021 \rangle$ -zone axis is calibrated using the  $1 \times 1 \times 2$  supercell of the monoclinic

phase, which has 24 atoms. Moreover, in STEM, the operational range is only  $\pm 23^\circ$ . As a result, we chose one featured grain with double-modulated stacking from the thinnest area of the focused ion beam (FIB) sample (Fig. S10 in the Supplemental Material [48]) and carefully aligned it to the crystal zone axis of  $\langle 021 \rangle$  for atomic-resolution imaging [Fig. 5(b)]. As mentioned before, our DFT calculations were only based on the fixed concentrations of dopant and  $V_O$  without surface, interface, or electrode. Thus, the middle parts of the monoclinic HZO grains were mainly focused on in our experiments. Interestingly, we found that the middle parts of the selected grain were effectively matched with  $M_1$  structures along the  $\langle 021 \rangle$ -direction [Figs. 5(c)–5(f)], while the parts close to the top and bottom TiN electrodes contain totally different structures due to their large angle deviations. Actually, the parent monoclinic structures of  $M_0$  and  $M_1$  are nearly the same but their oxygen configurations are different (Fig. S11 in the Supplemental Material [48]). Therefore, we undoubtedly need to choose dDPC instead of high-angle annular dark-field (HAADF) imaging to visualize the oxygen atomic columns in the crystal lattices.

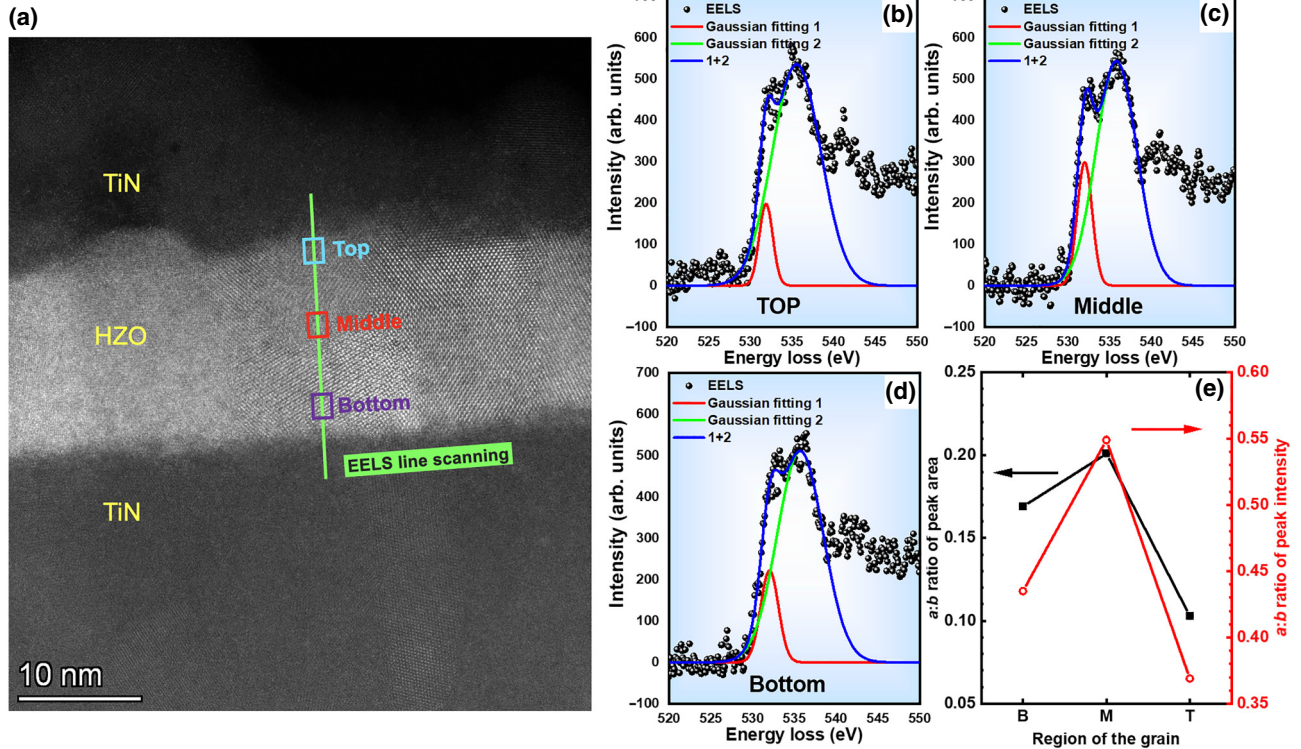


FIG. 6. EELS experiments for FE-HZO thin films. (a) HAADF image of the sample. EELS line scanning implemented along the green line. (b)–(d) O K EELS spectra of the three different regions given in (a) averaged across the TiN/FE-HZO/TiN stack. (e) Measured  $a:b$  ratio values of corresponding regions marked in (a). The calculated ratio value of  $a:b$  peak intensity increases from 0.44 to 0.55 and then decreases to 0.37 in O K edges when the line profile is across the stack, which implies that the oxygen vacancies mainly accumulate near the TiN electrodes. Note that the  $a:b$  ratio obtained from the peak area also shows the same trend.

To trace the distribution of  $V_O$  inside the FE-HZO layers, we conducted an EELS analysis of the O K edge for the FE-HZO layers (Fig. 6). From the EELS results, we further extracted the average O K spectra for three different regions in the FE-HZO layers [Fig. 6(a)]. In this case, the O K energy-loss near-edge structure of HZO also presents a characteristic doublet-peak shape denoted as peaks  $a$  and  $b$  [30,64]. According to previous reports, the formation of  $V_O$  reduces the first peak,  $a$ , intensity of the O K doublet edge when other factors are held constant [65,66]. Furthermore, the intensity peak ratio of  $a:b$  increases from 0.44 to 0.55 and then decreases to 0.37 in O K edges when the EELS line profile crosses the HZO layer [red curve in Fig. 6(e)], which suggests that  $V_O$  tend to accumulate close to the interface between the HZO layer and the TiN electrodes similar to previous reports [67,68]. It is noted that a comparable trend is obtained when performing a quantitative analysis on the peak area of  $a$  and  $b$  [black curve in Fig. 6(e) [48]].

To further discern  $V_O$  and its configuration, the atomically resolved STEM-iDPC/dDPC images of the aligned HZO grain were acquired. In particular, the middle parts of the selected grain [Fig. 5(b)], where monoclinic structures were mainly focused. Based on the  $\langle 021 \rangle$ -oriented  $M_1$

atomic model, the HAADF and then the dDPC simulations were performed to help understand the experimental results [Fig. 7(a)]. Owing to the  $Z$ -contrast nature of HAADF imaging (where  $Z$  is the atomic number), the intensity increases as the total number of atoms and/or their atomic number increase in each column [61,69]. Thus, the brightest spots in the HAADF images [Figs. 7(a-i) and 7(b)] are the Hf/Zr sites. The interstitial oxygen atomic columns cannot be directly observed via HAADF due to their very weak electron scattering [61]. Instead, oxygen atomic columns can be visible along with the heavy Hf/Zr elements in both iDPC [Fig. S12 in the Supplemental Material [48]] and dDPC images [Figs. 7(a-ii) and 7(c)]. Owing to the much lower atomic number, the interstitial oxygen atomic columns show a weaker image intensity compared with Hf/Zr in both iDPC and dDPC images [62]. In our case, however, the image quality of iDPC is worse than that of dDPC even after being Wiener filtered (Fig. S12 in the Supplemental Material [48]). Hence, the image contrast of dDPC was further inverted and shown in false color for improved visualization of the interstitial oxygen configuration.

The dDPC simulations based on the atomic structures of  $M_1$  along the  $\langle 021 \rangle$ -direction can be used to determine

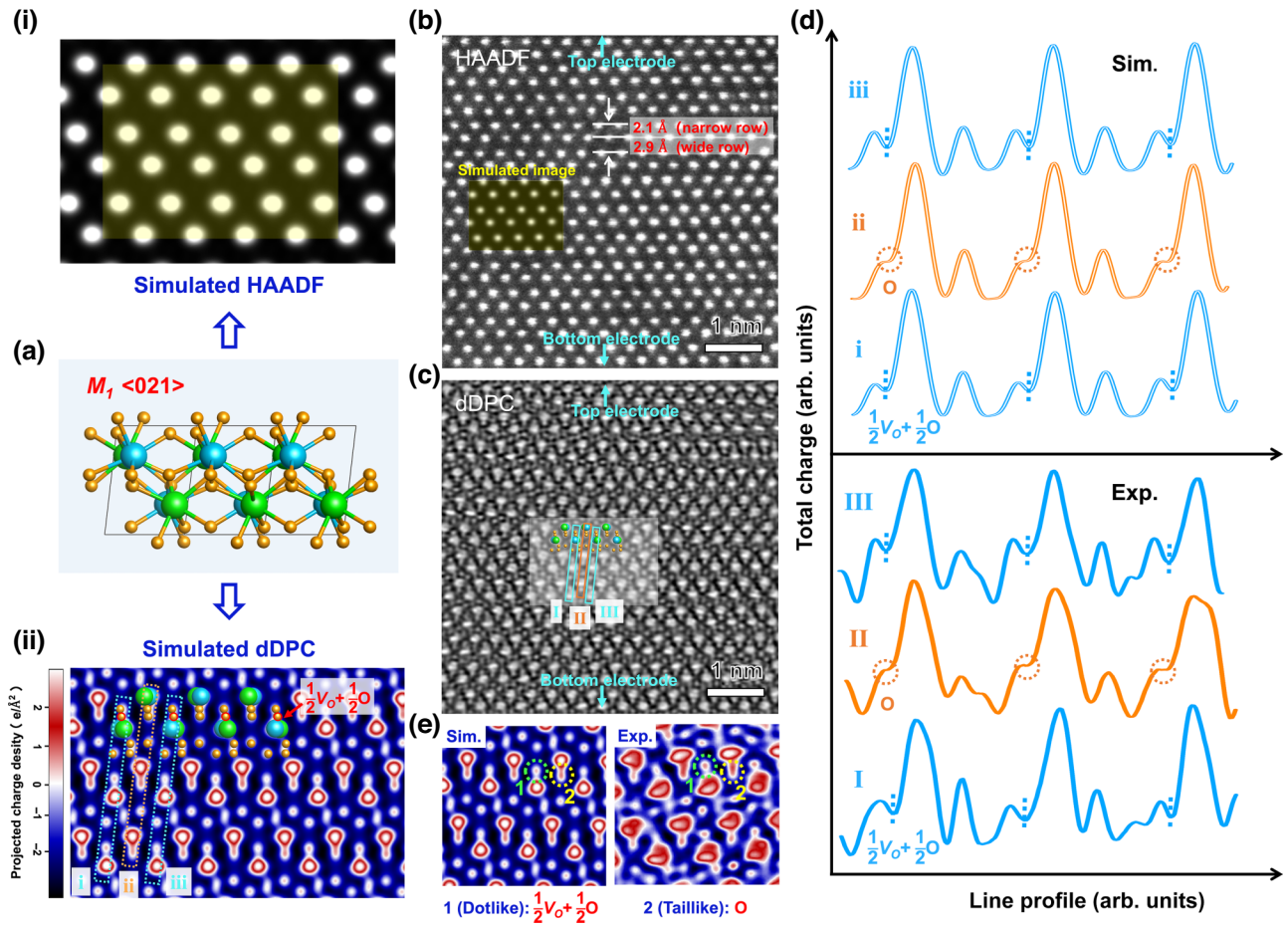


FIG. 7. Detection of  $M_1$  structures with ordered  $V_O$  in the aligned grain through an atomic-resolved dDPC image. (a) Atomic model of  $M_1$  structures along the  $\langle 021 \rangle$ -direction. (i)–(ii) Simulated HAADF image and the false-colored dDPC simulations calculated using the  $\langle 021 \rangle$ -oriented  $M_1$  model, respectively. In (a-ii), the corresponding atomic models are overlaid and the positions of the red circle indicate the sites of oxygen vacancy ( $V_O$ ). (b) Experimentally acquired HAADF image of the middle parts of the aligned grain in Fig. 5(b) [the image was tailored from the middle part of the image shown in Fig. 5(b)]. Inset is the corresponding HAADF simulations taken from (a-i). The narrow and wide rows are also indicated. (c) Filtered dDPC image with inverted contrast, in which the interstitial oxygen columns can be visible. The  $\langle 021 \rangle$ -oriented  $M_1$  model is overlaid to guide line profile drawing. Note that the top and bottom TiN electrode positions in (b),(c) are indicated by the turquoise arrows. (d) Results of the line profile taken along corresponding regions highlighted with dashed lines and solid lines in (a-ii) and (c), in which the periodic variation of charge density at the anionic sites can be clearly seen (from the simulated image and experimental ones) for  $M_1$  structures. (e) Enlarged views of the columns taken from (a-ii) and (c), in which the false-colored image intensity changes to some dotlike rather taillike ones at the oxygen-deficient sites, demonstrating an excellent quantitative match between theory and experiment.

the local charge density in the interstitial columns in the selected monoclinic structures. With help from the overlaid atomic structures of  $\langle 021 \rangle$ -oriented  $M_1$  phase, the ordered  $V_O$  in the narrow ( $\sim 2.1$  Å in width) rows of the crystal lattices is clearly observed [Fig. 7(a-ii)]. Furthermore, line profiles of the respective charge densities across the interstitial planes in  $M_1$  structures are qualitatively compared between the simulated dDPC image and the experimental one [Fig. 7(d)]. The periodic variation of charge density at the anionic sites can be clearly seen for  $M_1$  structures. Namely, the charge density map from dDPC measurements effectively matches that from the DFT calculations: both exhibit similar charge density profiles. Actually, validation

of the dDPC measurements is performed by comparing the experimental observations of an interstitial unit cell with the total charge density map calculated using DFT calculations, which has been proven to be an effective method [70].

To better discern the sites of ordered  $V_O$ , the charge density map (both the simulated and experimental ones) was enlarged and it reveals that the charge intensity changes to some “dotlike” rather “taillike” ones at the oxygen-deficient sites, which confirms the difference of localized electrons in the interstitial columns in  $M_1$  structures [Fig. 7(e)]. Furthermore, we identified the polarization orientation in the selected grain (Fig. 8). The polarization



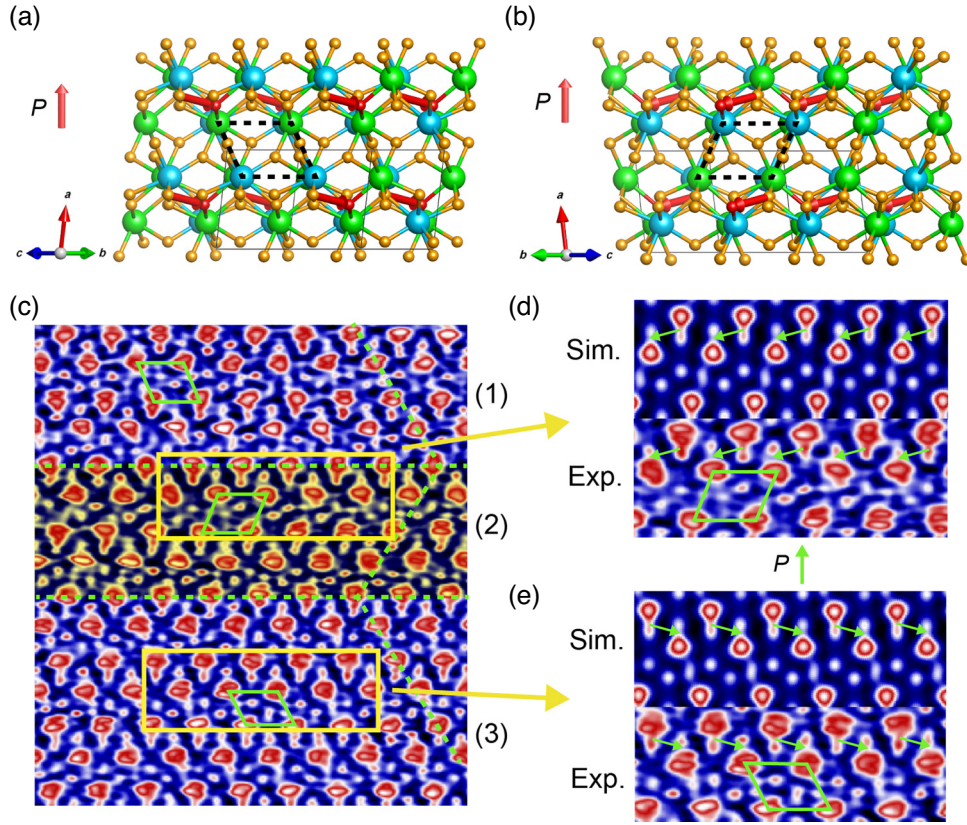


FIG. 8. Polarization orientation of the selected grain identified from the theoretical polarization of  $M_1$  structure. (a),(b) Structural models of the  $M_1$  phase oriented along the  $[02\bar{1}]$  and  $[021]$  directions, which can be distinguished by the half cell with large distortion highlighted by a dashed black parallelogram. These two models compose the twin structure in (c). The polarization is indicated using a red arrow. (c) Selected area of the target grain with a twin structure and different polarization directions. The green parallelograms highlight half cells with different orientations, which can be used to identify the twin structures. The dashed green lines are the twin boundaries and domain wall boundaries [three numbered regions have different polarizations, as shown in (d) and (e)]. (d),(e) Polarization of the selected regions (2) and (3) from (c). The upper part is the simulated dDPC image of the  $M_1$  phase and the lower part is the experimental dDPC image of the selected area. The polarization is depicted with a light green arrow.

of the selected grain in the dDPC image can be identified from the theoretical polarization of the  $M_1$  structure. It should be noted that the dDPC image is a projection onto the sample plane. Therefore, the polarization arrow depicted in Fig. 8 is a projected vector onto the sample plane. The  $M_1$  structures with different orientations in Figs. 8(a) and 8(b) compose the twin structure in Fig. 8(c), with the red arrows indicating polarization direction. From both the simulated and experimental charge density map in Figs. 8(d) and 8(e), the different vacancy arrangements with various polarization orientations can be identified. Grains with a monoclinic structure and ordered vacancies are also found in other samples, one of which is shown in Fig. S13 in the Supplemental Material [48]. Overall, the charge density map from dDPC measurements effectively matches that from simulations and DFT, intuitively confirming the presence of ferroelectric polar  $M_1$  structures in FE-HZO thin films.

## V. CONCLUSION

In summary, we proposed a mechanism involving ordered  $V_O$  in  $\text{HfO}_2$  that contributes to robust ferroelectricity through the formation of a stable ferroelectric phase via an order-disorder transition. To verify the proposed mechanism, we theoretically predicted a stable-polar  $M_1$  phase in the oxygen-deficient monocliniclike structure for  $\text{Hf}_{0.5}\text{Zr}_{0.5}\text{O}_{2-\delta}$ , in which two reversible states with the spontaneous polarization of  $27 \mu\text{C}/\text{cm}^2$  were calculated. We used  $C_S$ -corrected STEM to characterize the atomic structure of FE-HZO grains, which effectively corresponds with the theoretically predicted  $M_1$  structures. The consistency between experimental observations and theoretical calculations supports the proposed mechanism of  $V_O$ -ordering-induced ferroelectricity. The proposed mechanism and the corresponding theory calculation methods provide valuable insights into the origin of ferroelectricity

in HfO<sub>2</sub>-based ferroelectrics, which may open a new path for the exploitation of HfO<sub>2</sub>-based materials.

## ACKNOWLEDGMENTS

We thank B. Gao from Tsinghua University for the discussion about the oxygen vacancy ordering issues, Q. Luo from the Institute of Microelectronics (Chinese Academy of Sciences) for the preparation of ferroelectric HZO samples, W. Xi, C. Li, S.N. Yue, S.S. Liu, and R.R. Liu from the Center for Electron Microscopy in Tianjin University of Technology for the support with electron microscopy measurements and HRTEM/STEM data discussion, and L. Xie from Department of Physics, Southern University of Science and Technology, for image simulations and EELS/dDPC data discussion. This work was supported by the National Key Research and Development Program of China (Grant No. 2019YFB2205100) and the National Science Foundation of China (Grant No. 92064001).

J.F.K. conceived the idea and designed and supervised the project and F.L. designed and supervised the theoretical calculation of the project. H.L.M. executed the experiment part of the project, C.X.Y. executed the theoretical calculation part of the project, and M.Q.L. executed part of microscopy experiments under the direction of P.G., X.X.D., Y.D.Z., X.J.S., and F.C.L. W.W.Y. partly carried out the DFT calculations. H.L.L. tested the ferroelectric characteristics. J.X. and X.R.H. prepared the (S)TEM samples via a dual-beam FIB technique. J.M. Zhang assisted in (S)TEM operation. L.F.L. and P.H. partly supervised the project. J.F.K., F.L., H.L.M., C.X.Y., and M.Q.L. analyzed the data and co-wrote the manuscript. All the authors discussed the results and commented on the manuscript.

The authors declare that they have no competing interests.

## APPENDIX A: METHODS

### 1. HZO structure search

We used USPEX [46,47,71] code to search for the lowest energy phase of HZO with oxygen vacancies (Hf<sub>0.5</sub>Zr<sub>0.5</sub>O<sub>2- $\delta$</sub> ). As discussed in the main text, large oxygen vacancy concentration may lead to extensive leakage due to the large density of in-gap states. The density of in-gap states decreases as V<sub>O</sub> concentration decreases, as shown in Fig. S2 in the Supplemental Material [48]. We determined that vacancy concentration corresponding to  $\delta = 0.125$  is practical in HZO thin films. Therefore, we fixed the composition with  $\delta = 0.125$ . We used *m*-phase (space group *P2<sub>1</sub>/c*), *o*-phase (space group *Pca2<sub>1</sub>*), and *t*-phase (space group *P4<sub>2</sub>/nmc*) of the defect-free HfO<sub>2</sub> unit cells to construct oxygen-deficient HZO phase as seed structures to accelerate structure searching. We first substituted 50% of the Hf atoms to Zr atoms in a defect-free HfO<sub>2</sub> unit cell with 12 atoms, then made supercells with

24 atoms by expanding the unit cell in one of the three axis directions. Finally, one of the O atoms was removed to form an oxygen vacancy. We have accounted for all possible arrangements in the substitution and defect formation. These manually constructed structures are used as seed structures for the following structure-searching process. Structures with 23 atoms in the cell, corresponding to formula Hf<sub>4</sub>Zr<sub>4</sub>O<sub>15</sub>, were optimized iteratively using the evolutionary algorithm implemented in the USPEX code. For each generation, 60% of the structures with the lowest energy were used to produce the next generation, and 50 generations were simulated. Offspring structures in the next generation were produced using the following operators: heredity, soft mutation, permutation, random symmetric structure generator, and lattice mutation [49].

### 2. Structure relaxation and energy calculations

Structure relaxation and energy calculation of stoichiometric monoclinic *M*<sub>0</sub> phase and oxygen-deficient phases obtained by systematic structure searching (such as *M*<sub>1</sub>, *O*<sub>1</sub>, and *T*<sub>1</sub>) were carried out using VASP code [44,45] with the same simulation parameters. Species were treated using the projector-augmented plane wave method, with 5p<sup>6</sup>6s<sup>2</sup>5d<sup>2</sup> valence electron configuration for Hf and 4s<sup>2</sup>4p<sup>6</sup>5s<sup>2</sup>4d<sup>2</sup> for Zr and 2s<sup>2</sup>2p<sup>4</sup> for O. The plane wave cutoff energy was 520 eV and the Brillouin zone was sampled with gamma-centered k-point meshes with resolution  $0.04 \times 2 \pi \text{ \AA}^{-1}$ . Exchange-correlation energy was treated using the Perdew-Burke-Ernzerhof (PBE) function [72] and the comparison of PBE and other functions (PBEsol [73] and SCAN [74]) can be found in Fig. S5 in the Supplemental Material [48]. All the structures relaxed until the change of energy was less than 10<sup>-5</sup> eV between electron steps and less than 10<sup>-4</sup> eV between ionic steps. The structural data of *M*<sub>0</sub>, *M*<sub>1</sub>, *M*<sub>1</sub> (spatial reversal), *O*<sub>1</sub>, *T*<sub>1</sub>, and *DT*<sub>1</sub> phases (discussed in the main text) are listed in Tables S1–S6 in the Supplemental Material [48], respectively. The atomic structures of the six phases mentioned above are also given in Fig. S1 in the Supplemental Material [48].

### 3. Molecular dynamics simulations

We carried out an *ab initio* molecular dynamics (AIMD) simulation via CP2K [50] to confirm the thermal stability of the *M*<sub>1</sub> phase. The simulated structure is a  $2 \times 2 \times 1$  supercell of *M*<sub>1</sub> phase with 92 atoms. The PBE function [72] was used to treat exchange-correlation interaction and the pseudopotentials of Goedecker, Teter, and Hutter (GTH) [75] were used to describe the core electrons. Double- $\zeta$  split valence plus polarization Gaussian-type basis set was used to expand the Kohn–Sham orbitals and the plane wave cutoff was set to 600 Ry. The Brillouin zone was sampled with the  $\Gamma$  point. The Nose-Hoover thermostat [76,77] and barostat were used to simulate the NpT ensemble under temperature 300 K and pressure 0 GPa. The time

step for the simulation was set at 1 fs and the number of steps was 10 000 (10 ps).

#### 4. Transition path calculations

We used a solid-state nudged elastic band (SS-NEB) method to calculate the ferroelectric switching path of the  $M_1$  phase using the VTST package [53,54] and VASP code [44,45]. The climbing image method was used to find the highest energy image. The initial structure was an  $M_1$  phase unit cell, the final structure was a space reversal of the  $M_1$  phase, and the initial path was constructed by linear interpolating between initial and final structures. The path with seven images was optimized until the NEB force on each atom was less than  $10^{-2}$  eV/Å.

#### 5. Polarization calculations

Macroscopic polarization in dielectrics can be formulated in terms of the Berry phase according to the modern theory of polarization [78]. The path for the Berry phase calculation of the  $M_1$  phase is the same as the switching path calculated by the NEB method. The final structure is the space reversal of the initial structure, and the polarization of the final structure is half of the change of polarization along the path.

#### 6. Structure visualization

Crystalline structures in all the figures are plotted using VESTA software [79].

#### 7. Film deposition and device fabrication

The fabrication processes of TiN(30 nm)/Hf<sub>0.5</sub>Zr<sub>0.5</sub>O<sub>2-δ</sub> (15 nm)/TiN(40 nm) capacitors on p-doped Si (100) substrates are as follows. First, TiN bottom electrodes (BEs) of 40-nm thickness were formed by ion beam sputtering. Second, 15-nm-thick Hf<sub>0.5</sub>Zr<sub>0.5</sub>O<sub>2-δ</sub> thin films were deposited by atomic layer deposition (ALD) at 280 °C. We used Hf[N(C<sub>2</sub>H<sub>5</sub>)CH<sub>3</sub>]<sub>4</sub>, Zr[N(C<sub>2</sub>H<sub>5</sub>)CH<sub>3</sub>]<sub>4</sub>, and H<sub>2</sub>O as the Hf precursor, the Zr precursor, and the oxygen source, respectively. The Hf:Zr ratio was controlled by alternating deposition of one cycle of HfO<sub>2</sub> and one cycle of ZrO<sub>2</sub>; namely, an ALD cycle ratio of 1:1 (Hf-to-Zr precursor pulses) was applied to achieve a Zr content of 50% (cationic ratio of Zr:[Zr + Hf]) in the HfO<sub>2</sub> layers. Third, the top electrode TiN of 30-nm thickness was (ion beam) sputtered and patterned as rectangles with different sizes. Finally, the as-fabricated TiN/Hf<sub>0.5</sub>Zr<sub>0.5</sub>O<sub>2-δ</sub>/TiN ferroelectric capacitors were annealed for 30 s at 500 °C in a nitrogen atmosphere to crystallize the Hf<sub>0.5</sub>Zr<sub>0.5</sub>O<sub>2-δ</sub> thin films.

#### 8. Ferroelectric properties measurements

The ferroelectric hysteresis loop and further positive-up-negative-down (PUND) measurements were implemented

using a B1530A module in an Agilent B1500A semiconductor device analyzer. In addition, 1 KHz triangular wave and 250 Hz PUND pulse series were generated by a B1530A waveform generator/fast measurement unit (WGFMU) and applied on a 40 × 40 μm Hf<sub>0.5</sub>Zr<sub>0.5</sub>O<sub>2-δ</sub> ferroelectric stacks, with set and reset voltage amplitude ranging from 1 to 4 V. The charge density was calculated based on the transient current and integration time. An obvious hysteresis loop was also measured even after 10<sup>5</sup> set and reset cycles, which confirms the robust macroscopic ferroelectricity in the samples.

#### 9. HRTEM characterization

The annealed TiN/Hf<sub>0.5</sub>Zr<sub>0.5</sub>O<sub>2-δ</sub>/TiN capacitors were fabricated into a cross-section sample by using a dual-beam FIB technique in a FEI Helios G4 system, including the low-pressure polishing process at 5 and 2 keV, and then cleaned in Gatan 691 PIPS at 1–0.5 keV to remove the residual contamination and any possible damage. High-resolution transmission electron microscopy (HRTEM) was performed on an aberration-corrected (*C<sub>s</sub>*)-corrected FEI Themis electron microscope operated at 300 kV. HRTEM images were acquired at 460 000× magnification by using a CCD camera (Cete 2, FEI).

#### 10. STEM characterization

The atomic-resolution HAADF images of the targeted grain along ⟨021⟩-zone axes were obtained using a *C<sub>s</sub>*-corrected STEM instrument (FEI Titan Cubed Themis G2 300) at 300 kV with a probe convergence semiangle of ~21.4 mrad. The HAADF-STEM images were taken by an annular dark-field image detector with the inner semiangle larger than 79 mrad. The atomic-resolution integrated and differentiated differential phase contrast (iDPC and dDPC, respectively) STEM images were obtained under a *C<sub>s</sub>*-corrected STEM (FEI Titan Cubed Themis G2 300) operated at 300 kV with a convergence semiangle of 21.4 mrad. Four images used for 2D integration and differentiation were acquired by a 4-quadrant DF4 detector with an optional high-pass filter applied to reduce the low-frequency information in the image. The collection angles of iDPC and dDPC were set at 4–21 mrad.

#### 11. HRTEM image simulations

HRTEM images were simulated using the software package RECI<sub>PRO</sub> [80]. An electron with an accelerating voltage of 200 kV and spherical aberration *C<sub>s</sub>* = 1.2 mm was used throughout our simulation. The tilting angle, thickness of the sample, and the defocus value were varied from 0°–4°, 10–50 nm, and –10 ~ –50 nm, respectively. The zone axis of  $M_1$  and  $M_0$  were taken along the ⟨021⟩-direction. Due to the distortions induced by *V<sub>O</sub>* being so small, the comparative results could, thus, not

distinguish the  $M_1$  and  $M_0$  phases through the experimental measurement of HRTEM and even HRTEM image simulations.

## 12. HAADF and DPC image simulations

HAADF and DPC image simulations were carried out by using the software package DR. PROBE [81]. A 300-kV electron beam with a convergence angle of 25 mrad and a collection angle of 63–200 mrad for the HAADF detector was employed. The collection angle for the segmented detector was 6–23 mrad. The sample thickness is set at 5 nm. A probe size of  $\sim 0.04$  nm was also used to simulate the broadening due to effective beam size, thermal vibrations, and mechanical vibrations. The dDPC and iDPC images were directly calculated from the as-obtained DPC images.

## 13. Phase calibrations and error calculations

The interplane distance of two main lattice planes and the angle between them were chosen to implement the phase calibrations. The values obtained from the HRTEM and HAADF images (or corresponding FFT patterns) were compared. Normally, it is considered to be acceptable when errors of interplane distance are within 4% and the angle discrepancy is around  $1^\circ$ . Subsequently, comparison work for the atomic models along a particular zone axis with the experimental data was also undertaken. The errors of interplane distance can be calculated according to the following simple math formula:

$$\text{Errors} = \frac{\text{Measured Values} - \text{Calculated Values}}{\text{Calculated Values}} \times 100\%.$$

## 14. iDPC/dDPC-STEM image analysis methods

The iDPC and inverted dDPC are recently developed phase imaging techniques based on the center of mass movement of convergent electron beam diffraction patterns [61]. They are complementary to each other and are good approximations of their counterparts based on the center of mass. The iCOM and dCOM techniques are linear in phase and the Laplacian of the phase of the thin sample transmission function, respectively [62]. For very thin samples, the iDPC and inverted dDPC are linear in the projected electrostatic potential and the charge density distribution, respectively [61,63]. As a result, unlike the HAADF imaging, the interstitial light (e.g., oxygen) atoms close to the heavy atomic lattice can be visible. Owing to the much lower atomic order, the interstitial oxygen columns show a weaker image intensity compared with the Hf/Zr columns (Figs. 7 and S12 in the Supplemental Material [48]). In theory, noise suppression is best in iDPC, intermediate in DPC, and worst in dDPC. In our case, however, the experimental image quality of dDPC is improved compared

with that of iDPC (Fig. S12 in the Supplemental Material [48]). Based on the filtered dDPC image, false color was employed for improved visualization of the interstitial oxygen configuration (Fig. 7). To better understand the dDPC results, line profiles of the respective charge densities across the interstitial column in  $M_1$  structures are quantitatively compared between their simulated and experimental dDPC results [Fig. 7(d)].

## 15. EELS spectrum imaging (SI) analysis of the O K edge

The EELS spectra were first background-subtracted and then fitted by the nonlinear least-square (NLLS) method with the software package DIGITALMICROGRAPH. Two Gaussian functions were used to fit the EELS signals in an energy window of 525–540 eV.

## APPENDIX B: PHASE NAMING CONVENTIONS

Lowercase letters such as  $m$ ,  $o$ , and  $t$  refer to a general monoclinic, orthorhombic, and tetragonal phase, respectively. The  $dt$  phase is the distorted tetragonal phase with large lattice distortion. Uppercase letters are reserved for a specific phase; for example,  $M_1$  refers to a monoclinic phase with specific vacancy ordering.

In addition,  $M$  stands for monoclinic and the number represents the oxygen vacancy ordering. Specifically, the subscript 0 stands for no vacancies. For example,  $M_0$  stands for the monoclinic HZO phase with no vacancies, and  $M_1$  denotes the monoclinic HZO phase with vacancy ordering of the first type.

## APPENDIX C: POSSIBLE SWITCHING MECHANISM OF THE $M_1$ PHASE

The switching barrier in Fig. 4(b) is relatively high, while the real switching process may take a different path. In our proposed mechanism, ferroelectricity originates from the order-disorder transition of vacancies; therefore, the ferroelectric switching path may traverse through the disordered intermediate states. We found an energetically favored transition path (as depicted in Fig. S3 in the Supplemental Material [48]). The initial and final structures are  $2 \times 2 \times 1$  supercells ( $2 \times 2 \times 1 \times 23 = 92$  atoms) of the  $M_1$  phase. The vacancy concentration is kept the same as the unit cell of the  $M_1$  phase by constructing four vacancies in the  $2 \times 2 \times 1$  supercell. The polarization is switched by the displacements of the oxygen vacancies and the vacancies are switched one-by-one, during which the  $M_1$  phase goes through relatively disordered intermediate states and returns to the ordered state with the opposite polarization direction. The transition barrier is significantly lowered to about 25 meV/atom. In addition, charged vacancies have a lower diffusion barrier than neutral vacancies. The transition barrier is 15 meV/atom if every supercell has two

elementary charges. It should be noted that the size of the simulated system is limited by the computational cost of first-principles calculations and the real switching process may involve other mechanisms, such as generation and recombination of vacancies.

#### APPENDIX D: WAKEUP, FATIGUE, AND OTHER EFFECTS IN HfO<sub>2</sub>-BASED FERROELECTRIC FILMS

Wakeup, fatigue, and other effects of HfO<sub>2</sub>-based ferroelectric films can be explained within V<sub>O</sub>-formation theory. In pristine films, oxygen vacancies are randomly distributed (or disordered). During cycling, oxygen vacancies migrate under an applied electric field and become ordered, which causes an increase in spontaneous polarization. As the number of cycles increases, more vacancies are generated; this may cause the reappearance of central symmetry. Fatigue happens when the broken central symmetry is resumed, which leads to a decrease in polarization. The breakdown effect is associated with the formation of a conduction filament, which causes an increase in conductivity and electric breakdown. This mechanism is similar to the resistive switching in resistive random-access memory [82].

#### APPENDIX E: EFFECTS OF STRAIN, VACANCY CONCENTRATION, AND OTHER FACTORS ON PHASE STRUCTURE

The theoretical calculations in the main text assume a fixed V<sub>O</sub> concentration of 6.25%, fixed Zr doping concentration of 50%, zero strain, and no surface effects. This is the reason why we focus on the middle part of the selected grain. The part of the selected grain close to the electrodes is strongly affected by strain and surface effects and, therefore, may have a different phase structure compared with the middle part. In fact, phase calibration shows that the phase near the electrodes is not a monoclinic *M*<sub>1</sub> phase. Furthermore, the V<sub>O</sub> concentration close to the electrodes is also different, which can be seen from Fig. 6, in that the V<sub>O</sub> concentration near the electrodes is higher than that in the middle part. First-principles calculations, including nonideal factors, should be performed to obtain phase structure affected by these factors.

---

[1] T. Böske, J. Müller, D. Bräuhäus, U. Schröder, and U. Böttger, Ferroelectricity in hafnium oxide thin films, *Appl. Phys. Lett.* **99**, 102903 (2011).  
 [2] J. Müller, E. Yurchuk, T. Schlösser, J. Paul, R. Hoffmann, S. Müller, D. Martin, S. Slesazek, P. Polakowski, J. Sundqvist, M. Czernohorsky, K. Seidel, P. Kücher, R. Boschke, M. Trentzsch, K. Gebauer, U. Schröder, and T. Mikolajick, in *2012 Symposium on VLSI Technology (VLSIT)* (IEEE, 2012), pp. 25.

[3] A. Chernikova, M. Kozodaev, A. Markeev, D. Negrov, M. Spiridonov, S. Zarubin, O. Bak, P. Buragohain, H. Lu, and E. Suvorova, Ultrathin Hf<sub>0.5</sub>Zr<sub>0.5</sub>O<sub>2</sub> ferroelectric films on Si, *ACS Appl. Mater. Interfaces* **8**, 7232 (2016).  
 [4] M. H. Park, Y. H. Lee, H. J. Kim, Y. J. Kim, T. Moon, K. D. Kim, J. Mueller, A. Kersch, U. Schroeder, and T. Mikolajick, Ferroelectricity and antiferroelectricity of doped thin HfO<sub>2</sub>-based films, *Adv. Mater.* **27**, 1811 (2015).  
 [5] J. Okuno, T. Kunihiro, K. Konishi, H. Maemura, Y. Shuto, F. Sugaya, M. Materano, T. Ali, K. Kuehnel, K. Seidel, U. Schroeder, T. Mikolajick, M. Tsukamoto, and T. Umebayashi, in *2020 IEEE Symposium on VLSI Technology* (IEEE, 2020), pp. 1.  
 [6] Q. Luo, T. Gong, Y. Cheng, Q. Zhang, H. Yu, J. Yu, H. Ma, X. Xu, K. Huang, and X. Zhu, in *2018 IEEE International Electron Devices Meeting (IEDM)* (IEEE, 2018), pp. 2.6.1.  
 [7] S. S. Cheema, *et al.*, Enhanced ferroelectricity in ultrathin films grown directly on silicon, *Nature* **580**, 478 (2020).  
 [8] T. D. Huan, V. Sharma, G. A. Rossetti, and R. Ramprasad, Pathways towards ferroelectricity in hafnia, *Phys. Rev. B* **90**, 064111 (2014).  
 [9] R. Materlik, C. Künneth, and A. Kersch, The origin of ferroelectricity in Hf<sub>1-x</sub>Zr<sub>x</sub>O<sub>2</sub>: A computational investigation and a surface energy model, *J. Appl. Phys.* **117**, 134109 (2015).  
 [10] X. Sang, E. D. Grimley, T. Schenk, U. Schroeder, and J. M. LeBeau, On the structural origins of ferroelectricity in HfO<sub>2</sub> thin films, *Appl. Phys. Lett.* **106**, 162905 (2015).  
 [11] H.-J. Lee, M. Lee, K. Lee, J. Jo, H. Yang, Y. Kim, S. C. Chae, U. Waghmare, and J. H. Lee, Scale-free ferroelectricity induced by flat phonon bands in HfO<sub>2</sub>, *Science* **369**, 1343 (2020).  
 [12] J. Müller, T. S. Böske, U. Schröder, S. Mueller, D. Bräuhäus, U. Böttger, L. Frey, and T. Mikolajick, Ferroelectricity in simple binary ZrO<sub>2</sub> and HfO<sub>2</sub>, *Nano Lett.* **12**, 4318 (2012).  
 [13] S. Mueller, J. Mueller, A. Singh, S. Riedel, J. Sundqvist, U. Schroeder, and T. Mikolajick, Incipient ferroelectricity in Al-doped HfO<sub>2</sub> thin films, *Adv. Funct. Mater.* **22**, 2412 (2012).  
 [14] X. Xu, F.-T. Huang, Y. Qi, S. Singh, K. M. Rabe, D. Obeyesekera, J. Yang, M.-W. Chu, and S.-W. Cheong, Kinetically stabilized ferroelectricity in bulk single-crystalline HfO<sub>2</sub>: Y, *Nat. Mater.* **20**, 826 (2021).  
 [15] T. Kiguchi, T. Shiraiishi, T. Shimizu, H. Funakubo, and T. J. Konno, Domain orientation relationship of orthorhombic and coexisting monoclinic phases of YO<sub>1.5</sub>-doped HfO<sub>2</sub> epitaxial thin films, *Jpn. J. Appl. Phys.* **57**, 11UF16 (2018).  
 [16] T. Mimura, T. Shimizu, O. Sakata, and H. Funakubo, Large thermal hysteresis of ferroelectric transition in HfO<sub>2</sub>-based ferroelectric films, *Appl. Phys. Lett.* **118**, 112903 (2021).  
 [17] T. Schenk, C. M. Fancher, M. H. Park, C. Richter, C. Künneth, A. Kersch, J. L. Jones, T. Mikolajick, and U. Schroeder, On the origin of the large remanent polarization in La : HfO<sub>2</sub>, *Adv. Electron. Mater.* **5**, 1900303 (2019).  
 [18] U. Schroeder, E. Yurchuk, J. Muller, D. Martin, T. Schenk, P. Polakowski, C. Adelman, M. I. Popovici, S. V. Kalinin, and T. Mikolajick, Impact of different dopants on the switching properties of ferroelectric hafniumoxide, *Jpn. J. Appl. Phys.* **53**, 85 (2014).

- [19] E. D. Grimley, T. Schenk, T. Mikolajick, U. Schroeder, and J. M. LeBeau, Atomic structure of domain and interphase boundaries in ferroelectric HfO<sub>2</sub>, *Adv. Mater. Interfaces* **5**, 1701258 (2018).
- [20] M. H. Park, Y. H. Lee, H. J. Kim, T. Schenk, W. Lee, K. D. Kim, F. P. G. Fengler, T. Mikolajick, U. Schroeder, and C. S. Hwang, Surface and grain boundary energy as the key enabler of ferroelectricity in nanoscale hafnia-zirconia: a comparison of model and experiment, *Nanoscale* **9**, 9973 (2017).
- [21] M. Hyuk Park, H. Joon Kim, Y. Jin Kim, T. Moon, and C. Seong Hwang, The effects of crystallographic orientation and strain of thin Hf<sub>0.5</sub>Zr<sub>0.5</sub>O<sub>2</sub> film on its ferroelectricity, *Appl. Phys. Lett.* **104**, 072901 (2014).
- [22] R. R. Cao, Y. Wang, S. J. Zhao, Y. Yang, X. L. Zhao, W. Wang, X. M. Zhang, H. B. Lv, Q. Liu, and M. Liu, Effects of capping electrode on ferroelectric properties of Hf<sub>0.5</sub>Zr<sub>0.5</sub>O<sub>2</sub> thin films, *IEEE Electron Device Lett.* **39**, 1207 (2018).
- [23] W. Hamouda, A. Pancotti, C. Lubin, L. Tortech, C. Richter, T. Mikolajick, U. Schroeder, and N. Barrett, Physical chemistry of the TiN/Hf<sub>0.5</sub>Zr<sub>0.5</sub>O<sub>2</sub> interface, *J. Appl. Phys.* **127**, 064105 (2020).
- [24] M. Hoffmann, U. Schroeder, T. Schenk, T. Shimizu, H. Funakubo, O. Sakata, D. Pohl, M. Drescher, C. Adelman, R. Materlik, A. Kersch, and T. Mikolajick, Stabilizing the ferroelectric phase in doped hafnium oxide, *J. Appl. Phys.* **118**, 072006 (2015).
- [25] S. Starschich, S. Menzel, and U. Böttger, Evidence for oxygen vacancies movement during wake-up in ferroelectric hafnium oxide, *Appl. Phys. Lett.* **108**, 032903 (2016).
- [26] P. J. Liao, Y. K. Chang, Y.-H. Lee, Y. M. Lin, S. H. Yeong, R. L. Hwang, V. Hou, C. H. Nien, R. Lu, and C. T. Lin, in *2021 Symposium on VLSI Technology* (IEEE, 2021), pp. 1.
- [27] M. D. Glinchuk, A. N. Morozovska, A. Lukowiak, W. Stręk, M. V. Silibin, D. V. Karpinsky, Y. Kim, and S. V. Kalinin, Possible electrochemical origin of ferroelectricity in HfO<sub>2</sub> thin films, *J. Alloys Compd.* **830**, 153628 (2020).
- [28] P. Nukala, M. Ahmadi, Y. Wei, S. de Graaf, E. Stylianidis, T. Chakraborty, S. Matzen, W. Zandbergen Henny, A. Björling, D. Mannix, D. Carbone, B. Kooi, and B. Noheda, Reversible oxygen migration and phase transitions in hafnia-based ferroelectric devices, *Science* **372**, 630 (2021).
- [29] K. Z. Rushchanskii, S. Blügel, and M. Ležaić, Ordering of oxygen vacancies and related ferroelectric properties in HfO<sub>2-δ</sub>, *Phys. Rev. Lett.* **127**, 087602 (2021).
- [30] S. Kang, *et al.*, Highly enhanced ferroelectricity in HfO<sub>2</sub>-based ferroelectric thin film by light ion bombardment, *Science* **376**, 731 (2022).
- [31] C. Liu, F. Liu, Q. Luo, P. Huang, X. Xu, H. Lv, Y. Zhao, X. Liu, and J. Kang, in *2018 IEEE International Electron Devices Meeting (IEDM)* (IEEE, 2018), pp. 16.4.1.
- [32] M. Hyuk Park, H. Joon Kim, Y. Jin Kim, W. Lee, T. Moon, and C. Seong Hwang, Evolution of phases and ferroelectric properties of thin Hf<sub>0.5</sub>Zr<sub>0.5</sub>O<sub>2</sub> films according to the thickness and annealing temperature, *Appl. Phys. Lett.* **102**, 242905 (2013).
- [33] T. Mimura, T. Shimizu, H. Uchida, O. Sakata, and H. Funakubo, Thickness-dependent crystal structure and electric properties of epitaxial ferroelectric Y<sub>2</sub>O<sub>3</sub>-HfO<sub>2</sub> films, *Appl. Phys. Lett.* **113**, 102901 (2018).
- [34] U. Schroeder, M. H. Park, T. Mikolajick, and C. S. Hwang, The fundamentals and applications of ferroelectric HfO<sub>2</sub>, *Nat. Rev. Mater.* **7**, 653 (2022).
- [35] Y. Wang, L. Tao, R. Guzman, Q. Luo, W. Zhou, Y. Yang, Y. Wei, Y. Liu, P. Jiang, Y. Chen, S. Lv, Y. Ding, W. Wei, T. Gong, Y. Wang, Q. Liu, S. Du, and M. Liu, A stable rhombohedral phase in ferroelectric Hf(Zr)<sub>1+x</sub>O<sub>2</sub> capacitor with ultralow coercive field, *Science* **381**, 558 (2023).
- [36] M. Pešić, F. P. G. Fengler, L. Larcher, A. Padovani, T. Schenk, E. D. Grimley, X. Sang, J. M. LeBeau, S. Slesazeck, U. Schroeder, and T. Mikolajick, Physical mechanisms behind the field-cycling behavior of HfO<sub>2</sub>-based ferroelectric capacitors, *Adv. Funct. Mater.* **26**, 4601 (2016).
- [37] J. X. Zheng, G. Ceder, T. Maxisch, W. K. Chim, and W. K. Choi, First-principles study of native point defects in hafnia and zirconia, *Phys. Rev. B* **75**, 104112 (2007).
- [38] A. S. Foster, F. Lopez Gejo, A. L. Shluger, and R. M. Nieminen, Vacancy and interstitial defects in hafnia, *Phys. Rev. B* **65**, 174117 (2002).
- [39] J. C. Slater, Theory of the transition in KH<sub>2</sub>PO<sub>4</sub>, *J. Chem. Phys.* **9**, 16 (1941).
- [40] R. A. Cowley, Structural phase transitions I. Landau theory, *Adv. Phys.* **29**, 1 (1980).
- [41] B. E. Vugmeister and M. D. Glinchuk, Dipole glass and ferroelectricity in random-site electric dipole systems, *Rev. Mod. Phys.* **62**, 993 (1990).
- [42] D. Zhou, J. Xu, Q. Li, Y. Guan, F. Cao, X. Dong, J. Müller, T. Schenk, and U. Schröder, Wake-up effects in Si-doped hafnium oxide ferroelectric thin films, *Appl. Phys. Lett.* **103**, 192904 (2013).
- [43] A. F. Devonshire, Theory of ferroelectrics, *Adv. Phys.* **3**, 85 (1954).
- [44] G. Kresse and J. Hafner, Ab initio molecular dynamics for liquid metals, *Phys. Rev. B* **47**, 558 (1993).
- [45] G. Kresse and J. Furthmüller, Efficient iterative schemes for ab initio total-energy calculations using a plane-wave basis set, *Phys. Rev. B* **54**, 11169 (1996).
- [46] A. R. Oganov, A. O. Lyakhov, and M. Valle, How evolutionary crystal structure prediction works and why, *Acc. Chem. Res.* **44**, 227 (2011).
- [47] A. O. Lyakhov, A. R. Oganov, H. T. Stokes, and Q. Zhu, New developments in evolutionary structure prediction algorithm USPEX, *Comput. Phys. Commun.* **184**, 1172 (2013).
- [48] See Supplemental Material at <http://link.aps.org/supplemental/10.1103/PhysRevApplied.22.024028> for structural data, details of switching path, and additional experimental results.
- [49] P. V. Bushlanov, V. A. Blatov, and A. R. Oganov, Topology-based crystal structure generator, *Comput. Phys. Commun.* **236**, 1 (2019).
- [50] T. D. Kühne, *et al.*, CP2K: An electronic structure and molecular dynamics software package - Quickstep: Efficient and accurate electronic structure calculations, *J. Chem. Phys.* **152**, 194103 (2020).
- [51] M. Pesic, C. Kunneth, M. Hoffmann, H. Mulaosmanovic, S. Muller, E. T. Breyer, U. Schroeder, A. Kersch, T. Mikolajick, and S. Slesazeck, A computational study

- of hafnia-based ferroelectric memories: from ab initio via physical modeling to circuit models of ferroelectric device, *J. Comput. Electron.* **16**, 1236 (2017).
- [52] P. Fan, Y. K. Zhang, Q. Yang, J. Jiang, L. M. Jiang, M. Liao, and Y. C. Zhou, Origin of the intrinsic ferroelectricity of HfO<sub>2</sub> from ab initio molecular dynamics, *J. Phys. Chem. C* **123**, 21743 (2019).
- [53] G. Henkelman, B. P. Uberuaga, and H. Jónsson, A climbing image nudged elastic band method for finding saddle points and minimum energy paths, *J. Chem. Phys.* **113**, 9901 (2000).
- [54] G. Henkelman and H. Jónsson, Improved tangent estimate in the nudged elastic band method for finding minimum energy paths and saddle points, *J. Chem. Phys.* **113**, 9978 (2000).
- [55] R. He, H. Wu, S. Liu, H. Liu, and Z. Zhong, Ferroelectric structural transition in hafnium oxide induced by charged oxygen vacancies, *Phys. Rev. B* **104**, L180102 (2021).
- [56] L.-Y. Ma and S. Liu, Structural polymorphism kinetics promoted by charged oxygen vacancies in HfO<sub>2</sub>, *Phys. Rev. Lett.* **130**, 096801 (2023).
- [57] B. Max, M. Pešić, S. Slesazek, and T. Mikolajick, Interplay between ferroelectric and resistive switching in doped crystalline HfO<sub>2</sub>, *J. Appl. Phys.* **123**, 134102 (2018).
- [58] S. Starschich, S. Menzel, and U. Böttger, Pulse wake-up and breakdown investigation of ferroelectric yttrium doped HfO<sub>2</sub>, *J. Appl. Phys.* **121**, 154102 (2017).
- [59] Z. Fan, J. Xiao, J. Wang, L. Zhang, J. Deng, Z. Liu, Z. Dong, J. Wang, and J. Chen, Ferroelectricity and ferroelectric resistive switching in sputtered Hf<sub>0.5</sub>Zr<sub>0.5</sub>O<sub>2</sub> thin films, *Appl. Phys. Lett.* **108**, 232905 (2016).
- [60] Y. Cheng, Z. Gao, K. H. Ye, H. W. Park, Y. Zheng, Y. Zheng, J. Gao, M. H. Park, J.-H. Choi, K.-H. Xue, C. S. Hwang, and H. Lyu, Reversible transition between the polar and antipolar phases and its implications for wake-up and fatigue in HfO<sub>2</sub>-based ferroelectric thin film, *Nat. Commun.* **13**, 645 (2022).
- [61] B. Lin, X. Wu, L. Xie, Y. Kang, H. Du, F. Kang, J. Li, and L. Gan, Atomic imaging of subsurface interstitial hydrogen and insights into surface reactivity of palladium hydrides, *Angew. Chem., Int. Ed.* **59**, 20348 (2020).
- [62] I. Lazić, E. G. T. Bosch, and S. Lazar, Phase contrast STEM for thin samples: Integrated differential phase contrast, *Ultramicroscopy* **160**, 265 (2016).
- [63] L. Wang, R. Xie, B. Chen, X. Yu, J. Ma, C. Li, Z. Hu, X. Sun, C. Xu, S. Dong, T.-S. Chan, J. Luo, G. Cui, and L. Chen, In-situ visualization of the space-charge-layer effect on interfacial lithium-ion transport in all-solid-state batteries, *Nat. Commun.* **11**, 5889 (2020).
- [64] T. Mizoguchi, M. Saitoh, and Y. Ikuhara, First-principles calculation of oxygen K-electron energy loss near edge structure of HfO<sub>2</sub>, *J. Phys.: Condens. Matter* **21**, 104212 (2009).
- [65] G. D. Wilk and D. A. Muller, Correlation of annealing effects on local electronic structure and macroscopic electrical properties for HfO<sub>2</sub> deposited by atomic layer deposition, *Appl. Phys. Lett.* **83**, 3984 (2003).
- [66] S. Stemmer, Z. Q. Chen, W. J. Zhu, and T. P. Ma, Electron energy-loss spectroscopy study of thin film hafnium aluminates for novel gate dielectrics, *J. Microsc.* **210**, 74 (2003).
- [67] J. Lee, M. S. Song, W.-S. Jang, J. Byun, H. Lee, M. H. Park, J. Lee, Y.-M. Kim, S. C. Chae, and T. Choi, Modulating the ferroelectricity of hafnium zirconium oxide ultrathin films via interface engineering to control the oxygen vacancy distribution, *Adv. Mater. Interfaces* **9**, 2101647 (2022).
- [68] B. Sun, Y. X. Liu, L. F. Liu, N. Xu, Y. Wang, X. Y. Liu, R. Q. Han, and J. F. Kang, Highly uniform resistive switching characteristics of TiN/ZrO<sub>2</sub>/Pt memory devices, *J. Appl. Phys.* **105**, 061630 (2009).
- [69] S. D. Findlay, N. Shibata, H. Sawada, E. Okunishi, Y. Kondo, T. Yamamoto, and Y. Ikuhara, Robust atomic resolution imaging of light elements using scanning transmission electron microscopy, *Appl. Phys. Lett.* **95**, 191913 (2009).
- [70] Q. Zheng, T. Feng, J. A. Hachtel, R. Ishikawa, Y. Cheng, L. Daemen, J. Xing, J. C. Idrobo, J. Yan, N. Shibata, Y. Ikuhara, B. C. Sales, S. T. Pantelides, and M. Chi, Direct visualization of anionic electrons in an electrode reveals inhomogeneities, *Sci. Adv.* **7**, eabe6819 (2021).
- [71] A. R. Oganov and C. W. Glass, Crystal structure prediction using ab initio evolutionary techniques: Principles and applications, *J. Chem. Phys.* **124**, 244704 (2006).
- [72] J. P. Perdew, K. Burke, and M. Ernzerhof, Generalized gradient approximation made simple, *Phys. Rev. Lett.* **77**, 3865 (1996).
- [73] G. I. Csonka, J. P. Perdew, A. Ruzsinszky, P. H. T. Philipsen, S. Lebègue, J. Paier, O. A. Vydrov, and J. G. Ángyán, Assessing the performance of recent density functionals for bulk solids, *Phys. Rev. B* **79**, 155107 (2009).
- [74] J. Sun, A. Ruzsinszky, and J. P. Perdew, Strongly constrained and appropriately normed semilocal density functional, *Phys. Rev. Lett.* **115**, 036402 (2015).
- [75] S. Goedecker, M. Teter, and J. Hutter, Separable dual-space Gaussian pseudopotentials, *Phys. Rev. B* **54**, 1703 (1996).
- [76] S. Nosé, A unified formulation of the constant temperature molecular dynamics methods, *J. Chem. Phys.* **81**, 511 (1984).
- [77] W. G. Hoover, Canonical dynamics: Equilibrium phase-space distributions, *Phys. Rev. A* **31**, 1695 (1985).
- [78] R. Resta, Macroscopic polarization in crystalline dielectrics: the geometric phase approach, *Rev. Mod. Phys.* **66**, 899 (1994).
- [79] K. Momma and F. Izumi, VESTA 3 for three-dimensional visualization of crystal, volumetric and morphology data, *J. Appl. Crystallogr.* **44**, 1272 (2011).
- [80] Y. Seto and M. Ohtsuka, ReciPro: free and open-source multipurpose crystallographic software integrating a crystal model database and viewer, diffraction and microscopy simulators, and diffraction data analysis tools, *J. Appl. Crystallogr.* **55**, 397 (2022).
- [81] J. Barthel, Dr. Probe: A software for high-resolution STEM image simulation, *Ultramicroscopy* **193**, 1 (2018).
- [82] P. Huang, X. Y. Liu, W. H. Li, Y. X. Deng, B. Chen, Y. Lu, B. Gao, L. Zeng, K. L. Wei, G. Du, X. Zhang, and J. F. Kang, in *2012 International Electron Devices Meeting*, pp. 26.6.1.